JOURNAL OF CATALYSIS 128, 34–47 (1991)

Co-impregnated Rh/Al_2O_3

I. Preparation

J. S. HEPBURN,* H. G. STENGER, JR.,* AND C. E. LYMAN†

*Department of Chemical Engineering, †Department of Materials Science and Engineering, Lehigh University, Bethlehem, Pennsylvania 18015

Received April 16, 1990; revised August 24, 1990

The aqueous co-impregnation of rhodium trichloride with hydrofluoric acid (HF) into γ-alumina honeycombs is shown to be a reliable and predictable method for preparing catalysts with controlled distributions of metal. Electron probe microanalysis of these catalysts revealed that adding HF to the impregnating solution drove the Rh species beneath the external surface of the support into narrow egg-white bands. The objective of this work is to prepare a poison resistant catalyst which can be used for the reduction of nitric acid in flue gases. A multicomponent adsorption/exclusion model of the impregnation and drying steps of this catalyst preparation method is presented, and theoretical internal distributions are compared to experimentally measured Rh and F profiles. A good fit to the experimental Rh profiles was obtained using two adjustable parameters: the adsorption rate constant of the aqueous Rh species and the diffusivity of HF. All other parameters were experimentally determined, or reported in the literature. Simulated impregnation profiles were found to lend insight into the co-impregnation process. By comparing simulated catalyst profiles before and after drying, it was found that drying had a significant impact on determining the internal distribution of the deposited Rh. Although sharp Rh bands were formed during the impregnation step of preparation, the ultimate shape, height, and position of these buried layers of Rh were determined by the drying step.

INTRODUCTION

The major factor which determines the function of any catalyst is its chemical composition; however, for those catalysts consisting of an active ingredient dispersed within a porous carrier, the catalytic activity (*2, 3*), reaction selectivity (*4, 5*), and catalyst durability (*6, 7*) are often controlled by the internal distribution of the active ingredients within the support. For catalytic reactions with positive-order rate dependencies upon reactant concentration, distributions with the catalytically active material located near the support exterior (eggshell distribution) are often optimal (*8–10*). When selectivity or poisoning considerations are important or for reactions exhibiting negative-order rate dependencies upon reactant concentration, distributions with the active ingredient concentrated into subsurface layers (egg-white distribution) or subsurface cores (egg-yolk distributions) have been demonstrated to be superior (*11–14*).

The preparation of a supported catalyst with a prescribed internal concentration profile is not an easy task and often remains more of an art than a science (*1, 15*). For supported catalysts prepared by liquid-phase impregnation, one of the simplest ways of controlling the distribution of the active ingredient within the support is via co-impregnation. In co-impregnation, a second species (the co-impregnant) is added to the impregnating solution which contains the dissolved precursor of the active ingredient. During impregnation, the co-impregnant competes with the precursor for adsorption sites on the internal surface of the support. As the liquid proceeds into the pores, the less strongly adsorbed compo-

0021-9517/91 $3.00

nent is pushed ahead of the more strongly adsorbed one (8).

For a given precursor, eggshell (*16, 17*), egg-white, egg-yolk (*3, 9, 17–20*), or uniform (*3, 18, 21*) internal distributions of active ingredient can be produced by choosing different co-impregnants. Besides the nature of the precursor and co-impregnant, other parameters which influence the internal distribution of the catalytically active component include: (1) the method of impregnation (wet or dry), (2) the duration of the impregnation, (3) the nature of the support, and (4) the subsequent drying step.

Many authors (*8, 20, 22–24*) have developed theoretical models which attempt to describe this complex multicomponent adsorption/exclusion phenomena and have theoretically studied the factors which determine the internal distribution of deposited precursor within the support. The majority of these models (*20, 22, 23*) treat only the impregnation step of preparation and do not consider the drying step. It has been demonstrated by several investigators (*4, 8, 18, 23, 25, 26*) that the drying process plays a critical role in determining the resulting internal distribution of active ingredient within the support. Melo *et al.* (*24*) have considered both the impregnation and drying steps of preparation, and the review and theoretical treatment of these processes presented by Lee and Aris (8) are the most comprehensive. However, the drawback of these theoretical works is that none report experimental catalyst distributions which enable the model predictions to be quantitatively verified.

In the present work, aqueous rhodium chloride ($RhCl_3$) was co-impregnated with hydrofluoric acid (HF) into γ-alumina honeycombs of square cell geometry. Resulting internal distributions of Rh and F within the support were experimentally measured by electron probe microanalysis (EPMA). Multicomponent adsorption/exclusion models of the impregnation and drying steps of the preparation were developed and theoretically predicted catalyst profiles are compared to the experimentally measured internal distributions. The application of this catalyst preparation is for the reduction of nitric oxides in flue gases, where SO_2 poisoning of rhodium can occur. The ability to make an egg-yolk or egg-white distribution of rhodium in these catalysts could increase their tolerance to SO_2 poisoning. The goal of this work is to develop models which will allow the internal distribution of such a supported catalyst to be predicted prior to its preparation.

TABLE 1

Solution Concentrations

Catalyst	$RhCl_3$ (mol/cm^3)	HF (mol/cm^3)
A	3.8×10^{-5}	0
B	3.8×10^{-5}	3.3×10^{-3}
C	3.8×10^{-5}	6.6×10^{-3}
D	3.8×10^{-5}	9.9×10^{-3}

EXPERIMENTAL

Catalyst Preparation and Characterization

Following the procedure described previously (*17*), $RhCl_3(H_2O)_x$ (Aldrich Chemical Co.) was co-impregnated with HF under vacuum into dry γ-alumina honeycombs of square cell geometry (Corning Celcor EX78). Table 1 lists the impregnation solution concentrations for each catalyst (labeled A, B, C, and D) and Fig. 1 illustrates the impregnation apparatus. The honeycomb was a single cell (four walls) with a cell opening of 0.70 cm, a wall thickness of 0.12 cm, and a height of 2 cm. This honeycomb geometry and cell opening is typical of that used for selective catalytic reduction of NO_x in power plants. The properties of these supports are summarized in Table 2. Impregnation was allowed to proceed for 30 s. This amount of time was found to ensure complete imbibition of the solution but suppressed transport by diffusion. Immediately

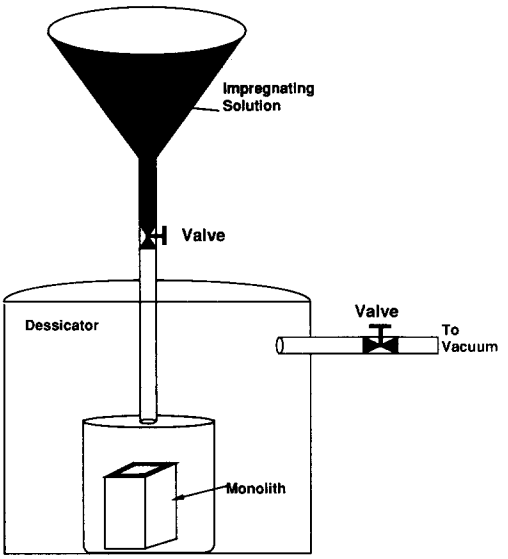

FIG. 1. Vacuum impregnation apparatus.

after impregnation, the honeycombs were dried in air for 1 h at 500°C.

A monolith wall was sectioned from the sample and placed in an epoxy mount alongside pure Rh and γ-alumina standards. The mounts were ground wet to 1 μm with silicon carbide paper, polished with 1-μm nap cloth, and given a clodiosilicate (particle size <0.25 μm) finish. This procedure enabled an externally flat surface to be obtained. The samples were then coated with a thin layer of evaporated carbon estimated to be about 10 nm thick.

Rh distributions were determined by X-ray emission spectroscopy (XES) with wavelength dispersive spectrometry (WDS) in a JEOL 733 EPMA with Tracor Northern automation (Model TN-2000/1310). At an accelerating voltage of 10 keV, the $L\alpha$ line of Rh and the $K\alpha$ line of Al were analyzed with PET and TAP crytals respectively. A defocused electron beam of approximately 10 μm in diameter was employed to average the effects of surface relief inherent in the porous alumina. Point counting was performed at 10-μm intervals along one wall of the honeycomb support. It was necessary to count for 120 s with a nominal probe current of 100 nA to obtain reasonable statistics (*27*) because the samples contained Rh loadings approaching the minimum detectability limits (*28*) of EPMA. Each analysis required approximately 6 h of probe time, 4 h for data collection at the 120 points, and 2 h for sample moving and alignment.

The catalyst which resulted from impregnating solution 3, catalyst C in Table 1, was analyzed for F by EPMA. Employing a polished CaF_2 crystal as a standard, the $K\alpha$ line of F was analyzed on a TAP crystal at an accelerating voltage of 5 keV. To curtail the effects of thermal loss and movement of the loosely bound F beneath the electron beam (*29*), point counting was performed for 20 s at 50-μm intervals with a 50-μm, 20-nA beam.

For both the Rh and F analyses, X-ray data was corrected for matrix effects using the atomic number correction of Duncumb and Reed (*30*), the absorption correction of Philibert (*31*), and fluorescence correction of Reed (*32*). Oxygen was calculated by difference because only one WDS spectrometer was equipped with the gas-flow proportional detector required for both Al and O X-ray detection. The resulting quantitative EPMA internal distributions of Rh have been presented and discussed in previous work (*17*).

TABLE 2

Support Properties

BET surface area	252	m^2/g
Pore volume	0.4949	cm^3/g
Porosity	0.63	
Density	1.31	g/cm^3
Wall thickness	1.2	mm
Cell density	9	cells/in^2

Adsorption Isotherms

In order to quantitatively interpret the adsorption of $RhCl_3$ and HF onto the γ-alumina support, Langmuir adsorption isotherms were determined by contacting given

quantities of crushed or powdered support (particle size <100 μm) with aqueous solutions of known $RhCl_3$ or HF concentration. The mixtures were stirred for a minimum of 5 days in order to establish equilibrium. The slurries were then filtered, and the filtrate concentrations determined by atomic absorption spectrophotometry (Perkin-Elmer Model 373) for $RhCl_3$ or with a solid-state fluoride electrode (Fisher Model 13-620-522) for HF. The amount of solute adsorbed onto the alumina was calculated from the difference between the initial and equilibrium solution concentrations.

THEORETICAL

Impregnation Model

The support is modeled as a collection of straight cylindrical pores with length L and radius R, where L is the distance from the outer surface of the support to its center, and R is given by

$$R = \frac{2\varepsilon}{\rho_s S} \tag{1}$$

(Symbols are defined in the nomenclature in the Appendix.) Initially, the pore volume of the support is evacuated; therefore, the rate at which impregnating solution is drawn into these pores can be approximated by the Washburn equation (*33*),

$$v_z = \frac{1}{2}\left(\frac{R\gamma}{2\mu t}\right)^{1/2} \quad or \quad \frac{dz_f}{dt} = \frac{R\gamma}{2\mu z_f}, \tag{2}$$

where z_f measures the penetration of the liquid front into the pore.

The continuity equations governing the simultaneous adsorption/desorption of n components on the internal surface of a pore during imbibition are given by

$$\frac{\partial C_j}{\partial t} + \alpha\frac{\partial n_j}{\partial t} = -v_z\frac{\partial C_j}{\partial z} \tag{3}$$

$$\frac{\partial n_j}{\partial t} = k_j^+ C_j\left(n_s - \sum_i n_i\right) - k_j^- n_j \tag{4}$$

$$C_j(0,z) = n_j(0,z) = 0 \tag{5}$$

$$C_j(t,0) = C_j^0, \tag{6}$$

where $z = 0$ at the pore inlet (support surface). These equations assume that diffusional transport and mass transfer resistances to adsorption are negligible. Equation (4) assumes that the adsorption of each species is independent of the other and that they adsorb onto the same type of site. Following the treatment described by Lee and Aris (*8*), this system of first-order hyperbolic equations can be transformed by the method of characteristics (*34*),

$$\frac{\partial C_j}{\partial z} = -\alpha\left(\frac{dz_f}{dt}\right)^{-1}\left(k_j^+ C_j\left(n_s - \sum_i n_j\right) - k_j^- n_j\right)$$

$$= \frac{-4\mu\alpha(z + A)}{R\gamma}\left(k_j^+ C_j\left(n_s - \sum_i n_i\right) - k_j^- n_j\right) \tag{7}$$

$$\frac{\partial n_j}{\partial A} = \left(\frac{dz_f}{dt}\right)^{-1}\left(k_j^+ C_j\left(n_s - \sum_i n_i\right) - k_j^- n_j\right)$$

$$= \frac{4\mu(z + A)}{R\gamma}\left(k_j^+ C_j\left(n_s - \sum_i n_i\right) - k_j^- n_j\right), \tag{8}$$

where

$$A = z_f - z \tag{9}$$

$$C_j(A,0) = C_j^0,\ n_j(0,z) = 0. \tag{10}$$

Drying Model

The continuity equations governing the simultaneous adsorption/desorption of n components on the internal surface of a pore during drying are given by:

$$\frac{\partial C_j}{\partial t} + \alpha\frac{\partial n_j}{\partial t} = D_j\frac{\partial^2 C_j}{\partial z^2} \tag{11}$$

$$\frac{\partial n_j}{\partial t} = k_j^+ C_j\left(n_s - \sum_i n_i\right) - k_j^- n_j. \tag{12}$$

If it is assumed that no redistribution due to diffusion takes place during the time between complete imbibition and the start of drying, the initial conditions for drying are the solutions from the impregnation model (Eqs. (7)–(10)).

It has been shown in previous work with

identical supports (*26*) that the drying process occurs completely in a falling rate regime at temperatures of 400°C and above. This implies that evaporation takes place at a moving interface at $z = z_f^{dry}$ beneath the external surface of the support. The boundary condition at this moving interface is given by

$$D_j \frac{\partial C_j}{\partial z} = -C_j \frac{dz_f^{dry}}{dt} + k_{mj}(p_j - p_j^o),\ z = z_f^{dry}. \quad (13)$$

Also, a solution for C_j must meet a condition of symmetry at the center of the support:

$$\frac{\partial C_j}{\partial z} = 0, \quad z = L. \quad (14)$$

This system of equations is a moving boundary problem. The moving boundary can be eliminated by the variable transformation

$$Y = \frac{L - z}{L - z_f^{dry}}. \quad (15)$$

The continuity equations (11) and (12) for the drying step then become

$$\frac{\partial C_j}{\partial t} = \frac{-Y}{(L - z_f^{dry})} \frac{dz_f^{dry}}{dt} \frac{\partial C_j}{\partial Y} + \frac{D_j}{(L - z_f^{dry})^2} \frac{\partial^2 C_j}{\partial Y^2} + \alpha k_j^- n_j - \alpha k_j^+ C_j \left(n_s - \sum_i n_i \right) \quad (16)$$

$$\frac{\partial n_j}{\partial t} = \frac{-Y}{(L - z_f^{dry})} \frac{dz_f^{dry}}{dt} \frac{\partial n_j}{\partial Y} + k_j^+ C_j \left(n_s - \sum_i n_i \right) - k_j^- n_j. \quad (17)$$

With the transformed boundary conditions as

$$C_j(0,Y) = C_j(A = 0,Y), \quad n_j(0,Y) = n_j(A = 0,Y) \quad (18)$$

$$\frac{\partial C_j}{\partial Y} = \frac{\partial n_j}{\partial Y} = 0, \quad Y = 0 \quad (19)$$

$$\frac{-D_j}{(L - z_f^{dry})} \frac{\partial C_j}{\partial Y} = -C_j \frac{dz_f^{dry}}{dt} + k_{mj}(p_j - p_j^o),\ Y = 1. \quad (20)$$

NUMERICAL ANALYSIS

Physical Parameters

The rate at which impregnating solution is drawn into the idealized support structure via capillary forces is calculated from properties that have been reported by the honeycomb manufacturer (Table 2). Using the BET surface area, $S = 252$ m^2/g and the support porosity of 0.63, the equivalent pore radius, R (Eq. (1)) is calculated to be 3.8 nm. This agrees well with the average pore radius reported by Corning of 4.1 nm, with a unimodal pore size distribution. The rate of penetration into a pore is subsequently obtained from Eq. (2). The impregnating solution viscosity, μ, and surface tension, γ, are assumed to be that of water at room temperature ($\mu = 0.01$ poise and $\gamma = 73.05$ dyn/cm^2).

Linearized plots of the $RhCl_3$ and HF Langmuir isotherms are shown in Fig. 2. From these plots the equilibrium adsorption constants, K_{RhCl_3} and K_{HF}, were determined to be 1.2×10^6 and 2.0×10^6 cm^3/mol, respectively. These agree well with values that have been reported by other researchers (*20*). Also from these data, the surface saturation concentrations of $RhCl_3$ and HF on the alumina were found to be 6.2×10^{-10} and 6.3×10^{-10} mole/cm^2, respectively. The closeness of these surface saturation constants helps verify the assumption that HF and $RhCl_3$ both adsorb onto the same type of site. For simplicity, an average surface saturation concentration, $n_s = 6.25 \times 10^{-10}$ mol/cm^2, was assumed for both species. For numerical analysis, a value of $k^+_{RhCl_3}$ was chosen, and k^+_{HF} calculated by assuming that $k^+_{RhCl_3}/k^+_{HF} = K_{RhCl_3}/K_{HF}$. When $k_1^+/k_2^+ = K_1/K_2$, the two-component adsorption problem approaches equilibrium monotonically, and numerical solutions to Eqs. (7) and (8) are better behaved (*1*).

Impregnation Model Solution

The boundary conditions for impregnation at $z = 0$, $C_j = C_j^o$, poses a problem. Experimental Rh loadings, which were de-

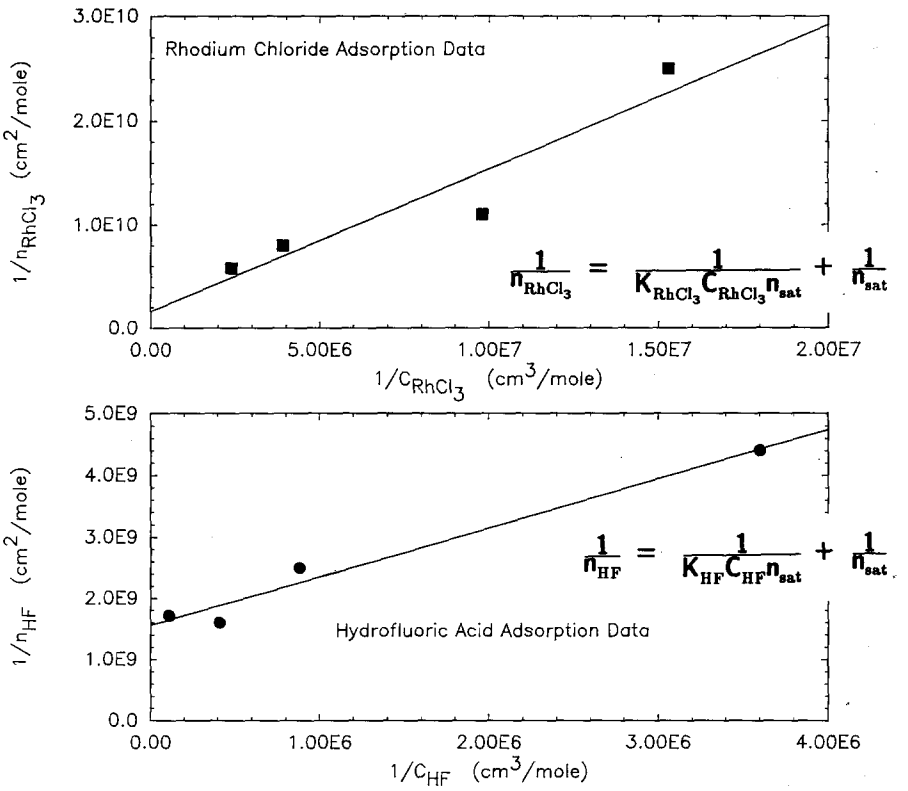

FIG. 2. Linearized adsorption isotherm data for HF and $RhCl_3$ on γ-alumina at 25°C.

termined by graphically integrating each catalyst's EPMA concentration profile across the width of the support, were approximately 50% lower than Rh loadings calculated by a Rh mass balance. It was shown in previous work (*17*) that the Rh loadings from EPMA were within 10% of independent analyses done by inductively coupled plasma emission spectroscopy. It was concluded in that work that pore mouth exclusion (*15*) was inhibiting a certain fraction of the $RhCl_3$ from entering the support. To allow the theoretical analysis to account for this exclusion, the bulk impregnation solution concentration of $RhCl_3$, $C^o_{RhCl_3}$, was corrected. For the subsequent numerical analyses, $C^o_{RhCl_3} = 1.7 \times 10^{-5}$ mol/cm^3 was used as the effective rhodium chloride concentration in the bulk liquid. Although this is a simplified method with which to address pour mouth exclusion, it allows satisfactory results for the present analysis. A more detailed model which includes pore mouth exclusion would be warranted if catalyst supports of differing pore size distribution were studied.

With their appropriate boundary conditions, Eqs. (7) and (8) were solved numerically on a Cyber 850 computer by a first-order explicit finite difference method. The numerical results of this system were used as initial conditions for the drying model. Except for the effective diffusivities of $RhCl_3$ and HF, all the parameters in the continuity equations for drying (Eqs. (11) and (12)) are fixed once $k^+_{RhCl_3}$ has been chosen for the impregnation model. An effective diffusion coefficient determined for rhodium trichloride in a similar alumina support ($D = 3.0 \times 10^{-6}$ cm^2/s) (*20*) was used for

D_{RhCl_3}. The effective diffusivity of HF, D_{HF}, was used as an adjustable parameter in the numerical analysis.

Drying Model Solution

Parameters in the drying boundary condition (Eq. (13) or (20)) for $z = z_f^{dry}$, include the unknowns dz_f^{dry}/dt, $k_{m,RhCl_3}$, $k_{m,HF}$, $p^o_{RhCl_3}$, and p^o_{HF}. Also p_{RhCl_3}, and p_{HF} are difficult to measure. The velocity of the drying front, dz_f^{dry}/dt, is calculated from the 500°C drying curve which was presented previously (*26*) as

$$\frac{dz_f^{dry}}{dt} = \frac{L}{\varepsilon}\frac{\rho_s}{\rho_{H_2O}}\frac{d}{dt}(m), \qquad (21)$$

where m is the moisture content (g H_2O/g support). A third-order polynomial,

$$\frac{dz_f^{dry}}{dt} = 2.5 \times 10^{-3} - 1.0 \times 10^{-4} t + 1.95 \times 10^{-6} t^2 + 1.5 \times 10^{-8} t^3 \text{ (cm/s)} \qquad (22)$$

was found to fit the drying data at 500°C accurately. If we assume that no volatile $RhCl_3$ species are produced during the drying process, then $p^o_{RhCl_3} = p_{RhCl_3} = 0$, and the boundary condition at $z = z_f^{dry}$ for $RhCl_3$ becomes

$$\frac{-D_{RhCl_3}}{(L - z_f^{dry})}\frac{\partial C_{RhCl_3}}{\partial Y} = -C_{RhCl_3}\frac{dz_f^{dry}}{dt}, \quad z = z_f^{dry}\,(Y = 1). \qquad (23)$$

The mass transfer coefficients for HF and H_2O, $k_{m,HF}$ and k_{m,H_2}, were approximated by knowing the flux of water at the surface of the shrinking liquid front and then assuming that the gas-phase mass transfer coefficient of HF was approximately the same as that of water. This assumption is likely since they are of similar atomic weight.

$$N_{H_2O} \approx -k_{m,H_2O}(p^s_{H_2O} - 0) = -k_{m,H_2O}P_T = -\frac{dz_f^{dry}}{dt}\frac{\rho^l_{H_2O}}{M_{w,H_2O}}. \qquad (24)$$

The partial pressure of water in the bulk gas surrounding the support is assumed to be small and is made equal to zero in Eq. (24). Also, since the evaporation process is rapid, the pores will be filled with essential 100% water vapor, thus $p^s_{H_2O} = P_T = 1$ atm. Also, if $k_{m,H_2O} \approx k_{m,HF}$, then

$$k_{m,HF} \approx \frac{dz_f^{dry}}{dt}\frac{\rho^l_{H_2O}}{M_{w,H_2O}}\frac{1}{P_T}. \qquad (25)$$

If it is assumed that HF vapor at the liquid–gas interface is in equilibrium with HF in the liquid phase, then the boundary condition for HF at $z = z_f^{dry}$ can be expressed

$$\frac{-D_{HF}}{(L - z_f^{dry})}\frac{\partial C_{HF}}{\partial Y} = -C_{HF}\frac{dz_f^{dry}}{dt} + \frac{K_{H,HF}C_{HF}}{P_T}\frac{dz_f^{dry}}{dt}, \; z = z_f^{dry}\,(Y = 1), \qquad (26)$$

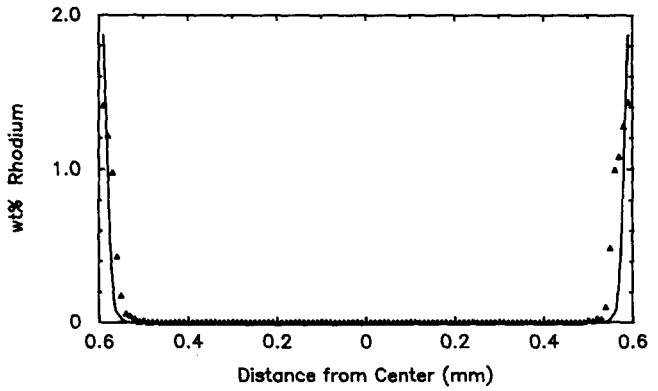

FIG. 3. Internal Rh distribution of catalyst A. Model is shown with line and EPMA data are points.

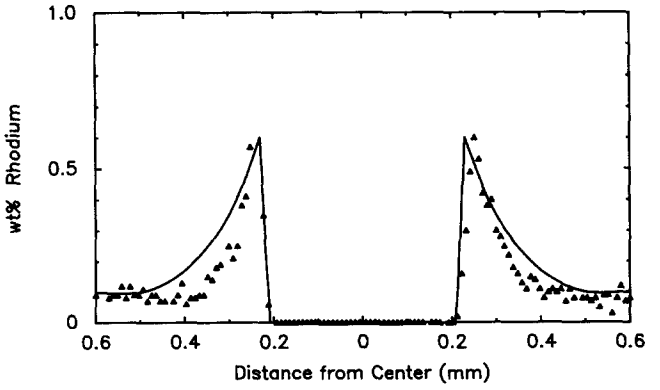

FIG. 4. Internal Rh distribution of catalyst B. Model is shown with line and EPMA data are points.

where $K_{H,HF} = p_{HF}/x_{HF}$. $K_{H,HF}$ is approximately 0.66 atm. at 100°C from thermodynamic data for HF available in the literature (*35*).

Equations (17) and (18) along with their appropriate boundary and initial conditions were solved numerically on a Cyber 850 computer using the DSS (*36*) partial differential equation package. The integration was ended when $z_f^{dry} = L$ at which point further redistribution of Rh and F was assumed not to occur.

RESULTS AND DISCUSSION

Numerically simulated internal Rh distributions are compared to those determined experimentally for catalysts A, B, C, and D in Figures 3, 4, 5, and 6 respectively. Even though the distributions are symmetrical, the entire wall crossection is shown to display the high degree of symmetry of the impregnation method. All four numerically generated Rh profiles were obtained with $k^+_{RhCl_3} = 6.6 \times 10^5$ cm^3/mol-s and $D_{HF} = 3.0 \times 10^{-6}$ cm^2/s. As discussed previously, all other parameters required for numerical simulation were either calculated using the previously described procedures, determined experimentally, or obtained from data available in the literature. These model parameters are summarized in Table 3. It should be noted that the prediction of the peak height is particularly sensitive to the chosen value of $k^+_{RhCl_3}$. Thus the determined

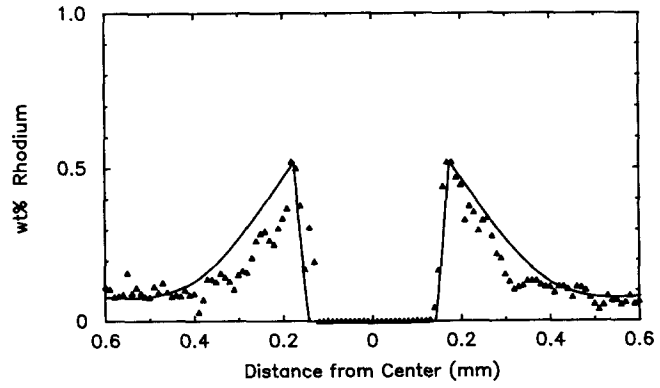

FIG. 5. Internal Rh distribution of catalyst C. Model is shown with line and EPMA data are points.

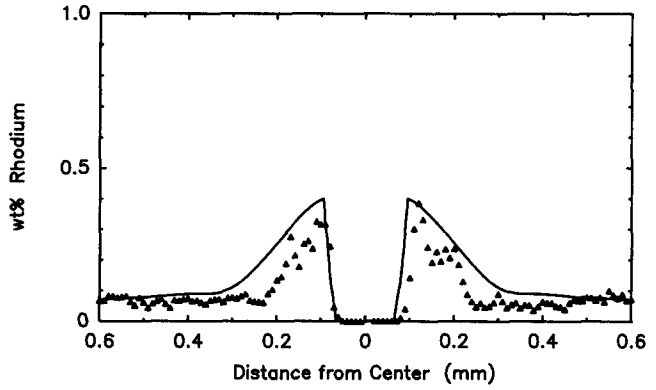

FIG. 6. Internal Rh distribution of catalyst D. Model is shown with line and EPMA data are points.

value of $6.6 \times 10^5 cm^3/mole\text{-}s$ should be considered an accurate representation of the rate of adsorption.

The accuracy of the numerical analyses was verified by comparing the average Rh loading (found by integrating the calculated Rh profile) to $v_p C_j^o$, where v_p is the pore volume of the support and C_j^o is the effective rhodium concentration in the bulk solution. The average error between these independent methods of determining the total rhodium in the catalyst was less than 7%. In Figs. 4, 5, and 6, the model overpredicts the local Rh concentration at positions located on the outer slopes of the Rh peaks. This is most likely due to errors in the numerical integration, since the continuity equations for both impregnation and drying are stiff and are difficult to numerically integrate in these regions.

TABLE 3

Model Parameters

R	3.8 nm
γ	73.05 dyn/cm^2
μ	0.01 poise
α	5.2×10^6 cm^{-1}
$k^+_{RhCl_3}$	6.6×10^5 cm^3/mol-s
k^+_{HF}	1.1×10^6 cm^3/mol-s
$k^-_{RhCl_3}$	0.55 s^{-1}
k^-_{HF}	0.55 s^{-1}
$C^o_{RhCl_3}$	1.7×10^{-5} mol/cm^3
n_s	6.25×10^{-10} mol/cm^2
L	0.06 cm
$K_{H,HF}$	0.661 atm
D_{RhCl_3}	3.0×10^{-6} cm^2/s
D_{HF}	3.0×10^{-6} cm^2/s

The internal distribution of fluorine for catalyst C is shown in Fig. 7. The numerical analysis simulates the fluorine profile well-but overpredicts the experimental F concentration by about 10%. Inaccuracies in the microanalysis could have occurred due to thermal loss and movement of the deposited fluorine underneath the electron beam of the EPMA. Also a certain fraction of the deposited fluorine could have been removed from the support surface, as HF or F_2, during the 500°C drying step.

Based on the success of the model for predicting the final rhodium and fluorine profiles in the monolith walls, it is expected that insight into the adsorption/exclusion process of co-impregnation can be gained by examining various parts of the computed solutions. Figures 8 and 9 show the calculated concentrations of $RhCl_3$ precursor in the liquid phase within the pores and the corresponding surface phase concentration of adsorbed Rh for catalysts B, C, and D. These plots are from the numerical simulation and represent the time when impregnation has stopped and drying is about to begin. These are valuable curves, since they

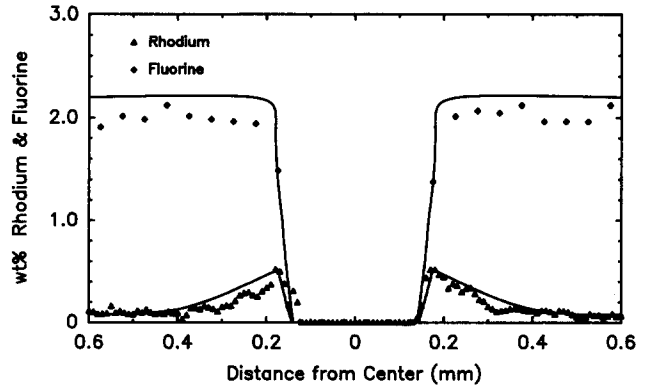

FIG. 7. Internal F distribution of catalyst C. Model is shown with line and EPMA data are points.

cannot be measured experimentally. In Fig. 8, the peak of $RhCl_3$ present in the liquid phase profile, corresponds exactly to the deposited $RhCl_3$ peak shown in Fig. 9. From testing the model's sensitivity, the height and sharpness of these peaks were found to be primarily controlled by the rate of adsorption of $RhCl_3$ and HF onto the support, while for a given concentration of HF in the impregnating solution, the distance that these peaks are driven beneath the external support surface is controlled by the surface saturation constant (n_s). Therefore to fit the experimental EPMA data, the adsorbed $RhCl_3$ (n_{RhCl_3}) peak height was controlled by adjusting $k^+_{RhCl_3}$ and the peak location was fixed by the n_s value which was determined independently.

Figure 9 shows that by increasing the concentration of HF in the impregnating solution from 3.3×10^{-3} to 9.9×10^{-3} mol/cm^3 (catalysts B to D), the $RhCl_3$ is only driven an additional 15 μm beneath the external surface of the support. Increasing the concentration of HF also causes the peak heights for both the dissolved and adsorbed $RhCl_3$ profile to decrease. This is attributed to the rate of imbibition being faster than the rate of adsorption of HF and $RhCl_3$ onto the support. If adsorption were much faster than the rate of imbibition (i.e., near-equilibrium

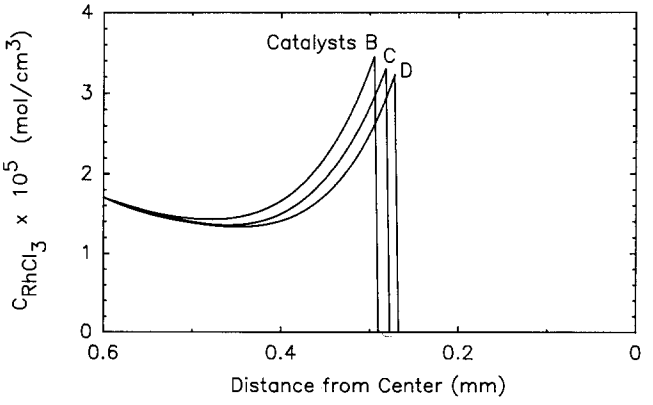

FIG. 8. Model prediction of the liquid phase $RhCl_3$ impregnation profiles within a pore for catalysts, B, C, and D, just following impregnation and just prior to drying.

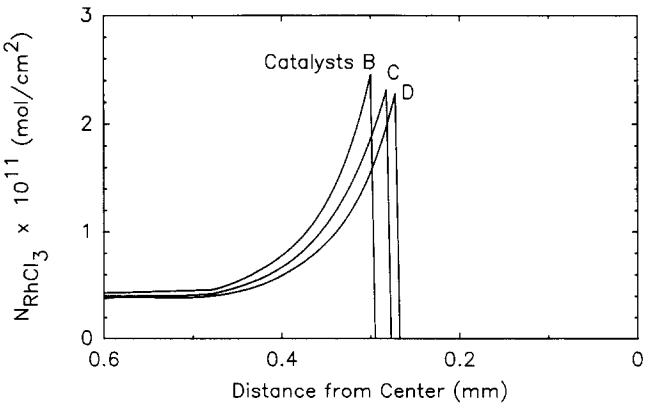

FIG. 9. Model prediction of the absorbed $RhCl_3$ impregnation profiles within a pore for catalysts B, C, and D, just following impregnation and just prior to drying.

adsorption), the $RhCl_3$ peaks would become sharper and increase in height as more HF is added to the impregnating solution. Simulated internal impregnation profiles of HF in the liquid phase and on the alumina surface are shown respectively in Figs. 10 and 11. These figures show that the HF penetrates exactly the same distance into the support as $RhCl_3$. This is expected since the imbibition rate is much greater than the diffusion rate of HF and $RhCl_3$.

The effect of drying in determining the internal distribution of deposited $RhCl_3$ is shown in Fig. 12. These plots are of the adsorbed rhodium. Thus the curves for before-drying show less total rhodium on the support than the curves for after-drying, because the after-drying curve includes the rhodium from the liquid which has adsorbed during drying. At an HF concentration of 3.3×10^{-3} mol/cm^3 in the impregnating solution (catalyst B), drying causes the Rh peak to be driven an additional 75 μm beneath the external surface of the support. The peak height is increased by approximately 0.07 wt% Rh but is less sharp than before drying. When the con-

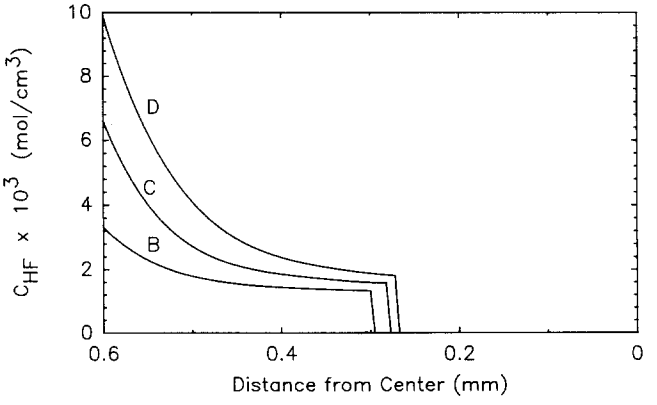

FIG. 10. Model prediction of the liquid phase HF impregnation profiles within a pore for catalysts B, C, and D, just following impregnation and just prior to drying.

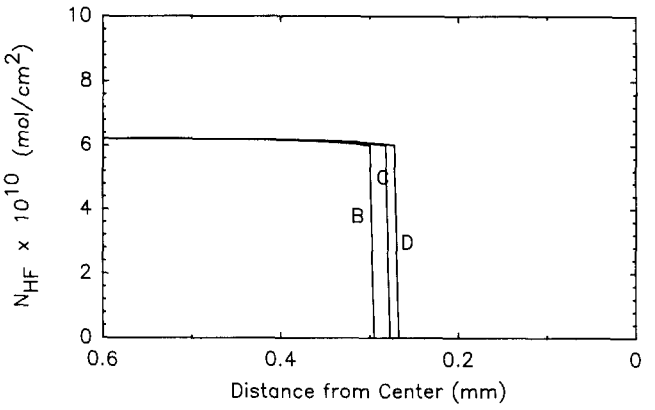

FIG. 11. Model prediction of adsorbed HF impregnation profiles within a pore for catalysts B, C, and D, just following impregnation and just prior to drying.

centration of HF in the impregnating solution is 6.6×10^{-3} (catalyst C), the Rh peak is driven an additional 110 μm beneath the support surface by drying, becomes less sharp, but retains a constant peak height. For the last catalyst made with 9.9×10^{-3} mol/cm^3 of HF (catalyst D), the Rh peak is driven 170 μm toward the support center by the drying process. However, the peak height is decreased by approximately 0.1 wt% Rh in this case and becomes much more diffuse. These results indicate that first drying causes a build-up of HF and $RhCl_3$ at the shrinking liquid front where evaporation is occuring. As this front moves toward the center of the support, the increase in HF and $RhCl_3$ concentrations in the liquid causes a competition for

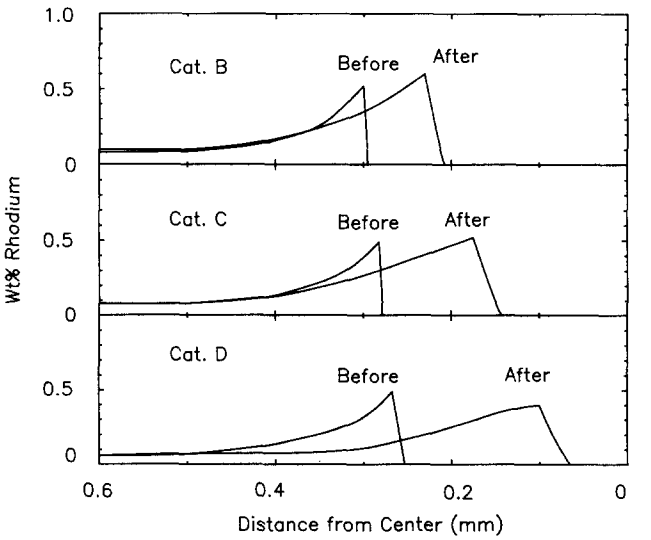

FIG. 12. Model prediction of the effects of drying on the Rh impregnation profile. These curves are of the adsorbed rhodium.

open adsorption sites on the support. The $RhCl_3$ is pushed ahead of the HF (toward the catalyst center) because HF adsorbs more strongly to the support than to the $RhCl_3$.

The tail on the Rh peaks near the center of the support is due to diffusion during drying. Drying is slower than impregnation, therefore the effects of diffusion become more observable during the drying step. With increasing concentrations of HF, the time required for all the HF and $RhCl_3$ to be deposited onto the support surface is a larger percentage of the total drying time. This effect makes the time for diffusion longer for the catalysts made with higher concentrations of HF and results in the more diffuse peaks shown in Fig. 12 for catalyst D. The decreased sharpness in the Rh peaks near the catalyst outer wall is believed to be due to HF evaporation.

CONCLUSION

Multicomponent adsorption/exclusion models of the impregnation and drying steps of catalyst preparation have been developed. Model simulations of the internal catalyst profiles compare quite well to experimentally determined internal Rh distributions which were obtained by the aqueous co-impregnation of $RhCl_3$ and HF into γ-alumina honeycombs. The proposed impregnation and drying models were found to fit the experimental EPMA Rh distributions using only two adjustable parameters (the adsorption rate constant for $RhCl_3$ and the diffusivity of HF). An experimentally measured fluorine concentration on the support was also found to agree within 10% of the model prediction. Based on a Rh material balance, an error of ~7% was found between the measured rhodium loading and the numerical integration of the model equations governing impregnation and drying. The predicted internal profiles for $RhCl_3$ and HF are shown to lend insight into the co-impregnation process. They revealed that drying plays a major role in forming the resulting Rh catalyst profiles. Drying was found to drive the Rh an additional 75 to 170 μm beneath the external surface of the support.

APPENDIX: SYMBOLS

C_j—Concentration of j in liquid phase (mol/cm^3)
C_j^o—Concentration of j in impregnating solution (mol/cm^3)
D_j—Effective diffusivity of j (cm^2/s)
k_{mj}—Mass transfer coefficient of j (mol/atm-s-cm^2)
k_j^+—Forward rate constant of j for kinetic adsorption (cm^3/s-mol)
k_j^-—Reverse rate constant of j for kinetic adsorption (1/s)
K_j—Equilibrium adsorption constant of j (cm^3/mol)
$K_{H,HF}$—Henrys law constant of HF (atm)
L—Distance from center to surface of support (cm)
$M_{w,j}$—Molecular weight of j (g/mol)
n_s—Surface saturation concentration (mol/cm^2)
n_j—Concentration of j on surface (mol/cm^2)
N_j—Flux of component j (mol/cm^2-s)
p_j—Partial pressure of j at interface (atm)
p_j^o—Partial pressure of j (atm)
P_T—Total pressure (atm)
R—Pore radius (cm)
S—Specific surface area (cm^2/g)
t—Time (s)
v_p—Pore volume of support (cm^3/g)
v_z—Velocity (cm/s)
x_j—Liquid phase mole fraction of j
z_f^{dry}—Drying front position (cm)
z_f—Impregnation front position (cm)

Greek

α—Surface area per unit pore volume (cm^2/cm^3)
γ—Surface tension (dyn/cm)
ε—Porosity
μ—Viscosity (g/sec-cm)
ρ_s—Support density (g/cm^3)
ρ_j^l—Liquid density of j (g/cm^3)

ACKNOWLEDGMENTS

This work was supported by the Department of Energy under contract DE-FG02-86ER45269 and by the Pennsylvania Energy Development Authority. Also, thanks is given to Corning Glass Works for the donation of the γ-alumina honeycombs.

REFERENCES

1. Lee, S. Y., PhD dissertation, University of Minnesota, 1981.
2. Roth, J. F., and Richard, T. E., *J. Res. Inst. Catal.* **20,** 85 (1972).
3. Michalko, E., U.S. Patent 3,259,589, July 5, 1968.
4. Yadzi, F. S., and Petersen, E. E., *Chem. Eng. Sci.* **27,** 227 (1972).
5. Corbett, W. E., and Luss, D., *Chem. Eng. Sci.* **29,** 1573 (1974).
6. Stenger, H. G., Meyer, E. C., Hepburn, J. S., and Lyman, C. E., *Chem. Eng. Sci.* **43,** 2067 (1988).
7. Hegedus, L. L., and Summers, J. C., *J. Catal.* **48,** 345 (1977).
8. Lee, S. Y., and Aris, R., *Catal. Rev. Sci. Eng.* **27,** 207 (1985).
9. Becker, E. R., and Nutall, T. A., "Preparation of Catalysts II—Proceedings of the 2nd International Symposium on the Scientific Bases for the Preparation of Heterogeneous Catalysts," p. 159. Elsevier, Amsterdam, 1979.
10. Vayenas, C. G., and Pavlou, S., *Chem. Eng. Sci.* **42**(7), 1655 (1987).
11. Bacaros, T., Bebelis, S., Pavlou, S., and Vayenas, C. G., "Catalyst Deactivation 1987," p. 459. Elsevier, Amsterdam, 1987.
12. Becker, E. R., and Wei, J., *J. Catal.* **46,** 365 (1977).
13. Becker, E. R., and Wei, J., *J. Catal.* **46,** 372 (1977).
14. Summers, J. C., and Hegedus, L. L., *J. Catal.* **51,** 185 (1978).
15. Neimark, A. V., Kheifez, L. I., and Fenelonov, V. B., *Ind. Eng. Chem. Prod. Res. Dev.* **20,** 439 (1981).
16. Maatman, R. W., and Prater, C. D., *Ind. Eng. Chem.* **49,** 253 (1957).
17. Hepburn, J. S., Stenger, H. G., and Lyman, C. E., *Appl. Catal.* **55,** 271 (1989).
18. Van den Berg, G. H., and Rijnten, H. T., *in* "Preparation of Catalysts II—Proceedings of the 2nd International Symposium on the Scientific Bases for the Preparation of Heterogeneous Catalysts," p. 159. Elsevier, Amsterdam, 1979.
19. Price, D. M., and Varma, A., *in* "AIChE Annual Meeting," paper 14c, New York, 1987.
20. Hegedus, L. L., Chou, T. S., Summers, J. C., and Potter, N. M., *in* "Preparation of Catalysts II," p. 171. Elsevier, Amsterdam, 1979.
21. Shyr, Y. S., and Ernst, W. R., *J. Catal.* **63,** 425 (1980).
22. Lobo, R., and Salmones, J., *in* "Proceedings of the 6th North American Meeting of the Catalysis Society, Chicago, 1979."
23. Komiyama, M., Merrill, R. P., and Harnsberger, H. F., *J. Catal.* **63,** 35 (1980).
24. Melo, F., Cervello, J., and Hermana, *Chem. Eng. Sci.* **35,** 2165 (1980).
25. Harriot, P., *J. Catal.* **14,** 43 (1969).
26. Hepburn, J. S., Stenger, H. G., and Lyman, C. E., *Appl. Catal.* **55,** 287 (1989).
27. Yakowitz, H., Vieth, D. L., Heinrich, K. F. J., and Michaelis, R. E., National Bureau of Standards, Spec. Pub. 260-10, 1965.
28. Ziebold, T. O., *Anal. Chem.* **39,** 858 (1967).
29. Goldstein, J. I., Newbury, D. E., Echlin, P., Joy, D. C., and Lifshin, E., "Scanning Electron Microscopy and X-ray Microanalysis." Plenum, New York, 1984.
30. Duncumb, P., and Reed, S. J. B., "Quantitative Electron Probe Microanalysis," p. 133. National Bureau of Standards Spec. Pub. 298, 1968.
31. Philibert, J., *in* Proc. 3rd Intl. Symp. X-Ray Optics and X-Ray Microanalysis, Stanford University, 1963," p. 379.
32. Reed, S. J. B., *Brit. J. Appl. Phys.* **16,** 913 (1965).
33. Washburn, E. W., *Phy. Rev.* **17,** 273 (1921).
34. Amundson, N. R., and Aris, R., "Mathematical Methods in Chemical Engineering," Vol. 2. Prentice–Hall, Englewood Cliffs, NJ, 1973.
35. *Nat. Petrol. News* **34,** 366 (1942).
36. Schiesser, W. E., "An Introduction to the Numerical Method of Lines Integration of Partial Differential Equations," Vol. 2. Lehigh University, 1977.